INTERNATIONAL JOURNAL FOR NUMERICAL METHODS IN ENGINEERING
Int. J. Numer. Meth. Engng 2008; **76**:1489–1512
Published online 19 June 2008 in Wiley InterScience (www.interscience.wiley.com). DOI: 10.1002/nme.2376

A contact algorithm for frictional crack propagation with the extended finite element method

Fushen Liu and Ronaldo I. Borja*, †

Department of Civil and Environmental Engineering, Stanford University, Stanford, CA 94305, U.S.A.

SUMMARY

We present an incremental quasi-static contact algorithm for path-dependent frictional crack propagation in the framework of the extended finite element (FE) method. The discrete formulation allows for the modeling of frictional contact independent of the FE mesh. Standard Coulomb plasticity model is introduced to model the frictional contact on the surface of discontinuity. The contact constraint is borrowed from non-linear contact mechanics and embedded within a localized element by penalty method. Newton–Raphson iteration with consistent linearization is used to advance the solution. We show the superior convergence performance of the proposed iterative method compared with a previously published algorithm called 'LATIN' for frictional crack propagation. Numerical examples include simulation of crack initiation and propagation in 2D plane strain with and without bulk plasticity. In the presence of bulk plasticity, the problem is also solved using an augmented Lagrangian procedure to demonstrate the efficacy and adequacy of the standard penalty solution. Copyright © 2008 John Wiley & Sons, Ltd.

Received 20 July 2007; Revised 1 April 2008; Accepted 2 April 2008

KEY WORDS: contact algorithm; frictional crack; extended finite element method

1. INTRODUCTION

Discontinuous deformation fields are encountered in a variety of engineering problems and manifest themselves in different forms [1–13]. Deformation bands are jumps in displacement gradients encountered in many natural and engineered materials. In metals they occur in the form of Lüders bands; in rocks they manifest themselves in the form of either compaction or dilation in combination with shearing. Cracks differ from deformation bands in that they create either a pair of free surfaces or a pair of contacting surfaces that slide past each other. Mode I cracking, for example, separates

*Correspondence to: Ronaldo I. Borja, Department of Civil and Environmental Engineering, Stanford University, Stanford, CA 94305, U.S.A.
†E-mail: borja@stanford.edu

Contract/grant sponsor: U.S. Department of Energy; contract/grant number: DE-FG02-03ER15454
Contract/grant sponsor: National Science Foundation; contract/grant number: CMG-0417521
Contract/grant sponsor: Stanford Graduate Fellowship

two parts of an initially continuous body into two regions and exposes a pair of traction-free surfaces. Modes II and III cracking, on the other hand, involve shearing on contacting surfaces. Tractions on the shear surfaces must be continuous to satisfy the equilibrium condition. In addition, some constitutive law must be satisfied relating the traction acting on the surface to the relative movement of the surfaces.

A challenging aspect of finite element (FE) modeling of crack nucleation and propagation lies in resolving the discontinuous displacement field within an element. A discontinuous displacement field defines the Dirac delta distribution function in the strain field, which in turn requires that the strain interpolation capability of a standard FE must be enhanced. Two types of techniques for enhancing the strain interpolation capability of a FE may be mentioned in this regard: local and global. In the local technique, a strong discontinuity, or displacement jump, is embedded inside the element along the direction of the crack. The enhancement is local in that the slip degree of freedom is eliminated on the element level, and so the enhancement has no effect on the global system of equations, see [14–21]. In the global approach, the slip degree of freedom is interpolated through the introduction of additional global degrees of freedom to existing nodes surrounding the crack. The latter class of methods are often called the extended FE methods [22–39]. A third class of approach, based on non-linear contact mechanics, applies to the case where the crack geometry is known *a priori* so that the element sides can be aligned to the crack [40–42]. Non-linear contact mechanics entails no enhancement to the element domain; rather, the enhancement is introduced to the element sides through some node-to-segment constitutive constraints.

This paper focuses on the extended FE method for modeling the problem of frictional crack propagation through elastic and elastoplastic bodies. A noteworthy feature of the approach is the variational formulation in terms of the relative displacement of contacting surfaces. The variational formulation gives rise to two independent equations: a standard variational equation without a discontinuity and a variational equation representing the enrichment needed to capture the discontinuity. The latter equation contains a surface integral that allows for the standard algorithm borrowed from non-linear contact mechanics to be embedded directly into the enriched FEs. We call our proposed algorithm 'self-contact' since the representation now consists of slave and master sides satisfying unilateral contact constraints, rather than the traditional slave node–master segment constraints of classical non-linear contact mechanics. Non-linear contact mechanics defines an evolution of state and deformation variables on a crack; hence, the extended FE approach pursued in this paper accommodates for path-dependent incremental loading, including forward and reverse loading.

We emphasize that although the variational equations for the global and local enrichment procedures look very similar, there are two key differences (apart from the degree of interpolation of slip). In the extended FE method, the weighting function for the auxiliary (enrichment) variational equation has the same form as that used for the trial function (standard Galerkin formulation), whereas in the local enrichment procedure, the weighting and trial functions are generally different (Petrov–Galerkin formulation). Furthermore, in the proposed extended FE framework the formulation accommodates for non-linear contact mechanics algorithm to be enforced on the crack, whereas in the local enrichment procedure the constitutive law on the crack is represented by the weighting function constructed for the auxiliary variational equation.

In the present formulation, non-linear contact mechanics algorithm is embedded into the variational equation by the penalty method. We realize that the penalty method may not be optimal for some problems since it could lead to poor conditioning of the system of equations in some cases. To address this concern, we also consider an augmented Lagrangian technique [43–45] and monitor

DOI: 10.1002/nme

the efficacy and adequacy of the standard penalty approach. For both the standard penalty and augmented Lagrangian procedures the FE equations allow the balance of linear momentum to be written in a standard residual form and linearized consistently for a full Newton–Raphson iteration. Linearization of the contact constraint is done simultaneously with linearization of the constraints imposed by bulk plasticity. The result is an iterative algorithm that preserves the asymptotic rate of quadratic convergence of Newton's method. We present numerical examples to demonstrate the performance of the proposed technique in a variety of 2D plane strain problems.

2. VARIATIONAL FORMULATION

Consider a body Ω with a surface of discontinuity $\mathscr{S}$ as shown in Figure 1. The surface $\mathscr{S}$ separates the body into subdomains Ω_+ and Ω_-. The displacement field $\mathbf{u}$ is discontinuous on $\mathscr{S}$ according to the equation

$$\mathbf{u}=\overline{\mathbf{u}}+M_{\mathscr{S}}(\mathbf{x})\widetilde{\mathbf{u}} \tag{1}$$

where $\overline{\mathbf{u}}$ and $M_{\mathscr{S}}(\mathbf{x})\widetilde{\mathbf{u}}$ are the continuous and discontinuous parts of $\mathbf{u}$, respectively. The scalar function $M_{\mathscr{S}}(\mathbf{x})$ generates the discontinuity on the surface $\mathscr{S}$ and is given by the equation

$$M_{\mathscr{S}}(\mathbf{x})=H_{\mathscr{S}}(\mathbf{x})-f^h(\mathbf{x}) \tag{2}$$

where $H_{\mathscr{S}}(\mathbf{x})$ is a Heaviside function defined by

$$H_{\mathscr{S}}(\mathbf{x})=\begin{cases}1, & \mathbf{x}\in\Omega_+\\ 0, & \mathbf{x}\in\Omega_-\end{cases} \tag{3}$$

and $f^h(\mathbf{x})$ is any arbitrary smooth function that satisfies the requirements $f^h=0$ in $\Omega_-\backslash\Omega_-^h$, and $f=1$ in $\Omega_+\backslash\Omega_+^h$. The jump of $M_{\mathscr{S}}$ on $\mathscr{S}$ is $[\![M_{\mathscr{S}}]\!]=1$, and $M_{\mathscr{S}}=0$ on the surface $\mathscr{S}_\pm^h$ so that $\Omega^h=\Omega_+^h\cup\Omega_-^h$ serves as its compact support. The parameterization (1) is exactly as adapted in [14–17, 19–21].

We restrict the discussion to infinitesimal deformation and write the small strain tensor as

$$\boldsymbol{\varepsilon}=\nabla^{\mathrm{s}}\mathbf{u}=\nabla^{\mathrm{s}}\overline{\mathbf{u}}+H_{\mathscr{S}}(\mathbf{x})\nabla^{\mathrm{s}}\widetilde{\mathbf{u}}-\nabla^{\mathrm{s}}(f^h(\mathbf{x})\widetilde{\mathbf{u}})+\delta_{\mathscr{S}}(\widetilde{\mathbf{u}}\otimes\mathbf{n})^{\mathrm{s}} \tag{4}$$

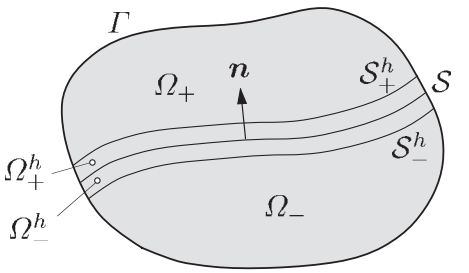

Figure 1. Definition of problem domain and boundaries. Domain Ω is cut by a surface of discontinuity $\mathscr{S}$ into Ω_- and Ω_+. Compact support of $M_{\mathscr{S}}(\mathbf{x})$ is $\Omega^h=\Omega_-^h\cup\Omega_+^h$ and bounded by surfaces $\mathscr{S}_\pm^h$. Unit normal vector to $\mathscr{S}$ is $\mathbf{n}$, pointing in the direction of Ω_+.

DOI: 10.1002/nme

where ∇^s is the symmetric spatial gradient operator, $(\cdot)^s$ denotes the symmetric part of the tensor, $\delta_{\mathscr{S}}$ is the Dirac delta distribution function, and $\mathbf{n}$ is the unit normal vector to $\mathscr{S}$ and pointing toward Ω_+. We remark that the above expression for the infinitesimal strain tensor has additional terms associated with $\nabla^s\widetilde{\mathbf{u}}$ arising from the gradient of the discontinuous part of $\mathbf{u}$, which has been ignored in the formulation of [14–17, 19–21].

Without loss of generality, we assume quasi-static loading and write the governing equations as follows:

$$\operatorname{div}(\boldsymbol{\sigma})+\mathbf{f}=\mathbf{0} \quad \text{in } \Omega\backslash\mathscr{S} \tag{5}$$

$$\boldsymbol{\nu}\cdot\boldsymbol{\sigma}=\mathbf{t} \quad \text{on } \Gamma_{\mathbf{t}} \tag{6}$$

where $\boldsymbol{\sigma}$ is the Cauchy stress tensor, $\mathbf{f}$ is the body force vector, $\mathbf{t}$ is the traction vector acting on the external surface boundary $\Gamma_{\mathbf{t}}$, and $\boldsymbol{\nu}$ is the unit normal vector to $\Gamma_{\mathbf{t}}$. We augment the above equations with the following conditions on the surface of discontinuity:

$$\mathbf{n}\cdot\boldsymbol{\sigma}=\mathbf{t}_{\mathscr{S}_-} \quad \text{on } \mathscr{S}_- \tag{7}$$

$$-\mathbf{n}\cdot\boldsymbol{\sigma}=\mathbf{t}_{\mathscr{S}_+} \quad \text{on } \mathscr{S}_+ \tag{8}$$

Consistent with the displacement field (1), we assume a family of weighting functions of the form

$$\boldsymbol{\eta}=\overline{\boldsymbol{\eta}}+M_{\mathscr{S}}(\mathbf{x})\widetilde{\boldsymbol{\eta}} \tag{9}$$

The standard variational formulation leads to an expression of the form

$$\int_\Omega \nabla^s\boldsymbol{\eta}:\boldsymbol{\sigma}\,\mathrm{d}\Omega=\int_\Omega \boldsymbol{\eta}\cdot\mathbf{f}\,\mathrm{d}\Omega+\int_\Gamma \boldsymbol{\eta}\cdot\mathbf{t}\,\mathrm{d}\Gamma \tag{10}$$

Substituting the weighting function (9) into (10) and using the definition of Dirac delta distribution function yield

$$\begin{aligned}&\int_\Omega [\nabla^s\overline{\boldsymbol{\eta}}+H_{\mathscr{S}}(\mathbf{x})\nabla^s\widetilde{\boldsymbol{\eta}}-\nabla^s(f^h(\mathbf{x})\widetilde{\boldsymbol{\eta}})]:\boldsymbol{\sigma}\,\mathrm{d}\Omega+\int_{\mathscr{S}}\widetilde{\boldsymbol{\eta}}\cdot\mathbf{t}_{\mathscr{S}_-}\,\mathrm{d}\Gamma\\ &\quad=\int_\Omega(\overline{\boldsymbol{\eta}}+M_{\mathscr{S}}(\mathbf{x})\widetilde{\boldsymbol{\eta}})\cdot\mathbf{f}\,\mathrm{d}\Omega+\int_\Gamma(\overline{\boldsymbol{\eta}}+M_{\mathscr{S}}(\mathbf{x})\widetilde{\boldsymbol{\eta}})\cdot\mathbf{t}\,\mathrm{d}\Gamma\end{aligned} \tag{11}$$

Since $\overline{\boldsymbol{\eta}}$ and $\widetilde{\boldsymbol{\eta}}$ are two independent weighting functions, we obtain independent variational equations

$$\int_\Omega \nabla^s\overline{\boldsymbol{\eta}}:\boldsymbol{\sigma}\,\mathrm{d}\Omega=\int_\Omega \overline{\boldsymbol{\eta}}\cdot\mathbf{f}\,\mathrm{d}\Omega+\int_\Gamma \overline{\boldsymbol{\eta}}\cdot\mathbf{t}\,\mathrm{d}\Gamma \tag{12}$$

and

$$\begin{aligned}&\int_\Omega [H_{\mathscr{S}}(\mathbf{x})\nabla^s\widetilde{\boldsymbol{\eta}}-\nabla^s(f^h(\mathbf{x})\widetilde{\boldsymbol{\eta}})]:\boldsymbol{\sigma}\,\mathrm{d}\Omega+\mathscr{G}_{\mathrm{c}}(\widetilde{\boldsymbol{\eta}},\mathbf{t}_{\mathscr{S}_-})\\ &\quad=\int_\Omega M_{\mathscr{S}}(\mathbf{x})\widetilde{\boldsymbol{\eta}}\cdot\mathbf{f}\,\mathrm{d}\Omega+\int_\Gamma M_{\mathscr{S}}(\mathbf{x})\widetilde{\boldsymbol{\eta}}\cdot\mathbf{t}\,\mathrm{d}\Gamma\end{aligned} \tag{13}$$

DOI: 10.1002/nme

where

$$\mathscr{G}_{\mathrm{c}}(\widetilde{\boldsymbol{\eta}}, \mathbf{t}_{\mathscr{S}_-}) = \int_{\mathscr{S}} \widetilde{\boldsymbol{\eta}} \cdot \mathbf{t}_{\mathscr{S}_-} \, \mathrm{d}\Gamma \tag{14}$$

is a surface integral arising from slip on the surface of discontinuity. Equation (12) is the standard variational equation without a discontinuity, whereas Equation (13) is the variational equation associated with the constraint on the discontinuity. Note that the region of integration for (13) is limited to the support of $M_{\mathscr{S}}(\mathbf{x})$, as can be seen from the fact that

$$H_{\mathscr{S}}(\mathbf{x}) \nabla^{\mathrm{s}} \widetilde{\boldsymbol{\eta}} - \nabla^{\mathrm{s}}(f^h(\mathbf{x}) \widetilde{\boldsymbol{\eta}}) = M_{\mathscr{S}}(\mathbf{x}) \nabla^{\mathrm{s}} \widetilde{\boldsymbol{\eta}} - (\widetilde{\boldsymbol{\eta}} \otimes \nabla f^h(\mathbf{x}))^{\mathrm{s}} \tag{15}$$

Since $f^h(\mathbf{x}) = 0, 1$ outside of the support Ω^h, the above expression vanishes in $\Omega \backslash \Omega^h$. Furthermore, Equation (14) requires a contact constitutive law governing slip on the surface of discontinuity, which we present in the following section.

3. SELF-CONTACT CONSTITUTIVE LAW

Since the surface of discontinuity $\mathscr{S}$ could cut through the interior of the FEs, the classical FE contact mechanics should be reformulated to reflect the so-called 'self-contact' kinematics. By self-contact we mean that the constitutive law on $\mathscr{S}$ should now be formulated in the interior of the element rather than at the nodes and sides of the FEs. The notion of 'slave' and 'master' nodes/segments of classical contact mechanics applies equally well to the present case, except that they now pertain to each side of $\mathscr{S}$. For the sake of definition, we assign Ω_+ as the slave side and Ω_- as the master side. The gap function on $\mathscr{S} \in \Omega$ is given by

$$g_{\mathrm{N}}(\mathbf{x}) = [\mathbf{u}_+(\mathbf{x}) - \mathbf{u}_-(\mathbf{x})] \cdot \mathbf{n}(\mathbf{x}) = \widetilde{\mathbf{u}}(\mathbf{x}) \cdot \mathbf{n}(\mathbf{x}), \quad \mathbf{x} \in \mathscr{S} \tag{16}$$

where $\mathbf{u}_+(\mathbf{x})$ and $\mathbf{u}_-(\mathbf{x})$ are the displacements at $\mathbf{x}$ interpreted to lie on the slave and master sides of $\mathscr{S}$, respectively. The relative tangential displacement vector is given by

$$\begin{aligned} \mathbf{g}_{\mathrm{T}}(\mathbf{x}) &= \sum_{\alpha=1}^{2} [\mathbf{u}_+(\mathbf{x}) - \mathbf{u}_-(\mathbf{x})] \cdot [\mathbf{m}_\alpha(\mathbf{x}) \otimes \mathbf{m}_\alpha(\mathbf{x})] \\ &= \sum_{\alpha=1}^{2} [\widetilde{\mathbf{u}}(\mathbf{x}) \cdot \mathbf{m}_\alpha(\mathbf{x})] \mathbf{m}_\alpha(\mathbf{x}), \quad \mathbf{x} \in \mathscr{S} \end{aligned} \tag{17}$$

where $(\mathbf{m}_1, \mathbf{m}_2, \mathbf{n})$ form three mutually orthogonal unit vectors. In 2D, the relative tangential movement simplifies to the scalar form

$$g_{\mathrm{T}}(\mathbf{x}) = \widetilde{\mathbf{u}}(\mathbf{x}) \cdot \mathbf{m}(\mathbf{x}), \quad \mathbf{x} \in \mathscr{S} \tag{18}$$

Contact condition on $\mathscr{S}$ is imposed in the normal direction through the standard Kuhn–Tucker relations

$$g_{\mathrm{N}} \geqslant 0, \quad t_{\mathrm{N}} \leqslant 0, \quad g_{\mathrm{N}} t_{\mathrm{N}} = 0, \quad t_{\mathrm{N}} = \mathbf{t}_{\mathscr{S}_-} \cdot \mathbf{n} \tag{19}$$

The component of traction, $-t_{\mathrm{N}}$, represents the contact pressure. We satisfy the gap condition if $g_{\mathrm{N}} > 0$ and $t_{\mathrm{N}} = 0$, and the contact condition if $g_{\mathrm{N}} = 0$ and $t_{\mathrm{N}} < 0$.

DOI: 10.1002/nme

In the tangential direction, we distinguish between stick and slip conditions, which are governed by a frictional constitutive law. Let the resolved tangential traction on $\mathscr{S}$ be given by

$$t_{\mathrm{T}} = \|\mathbf{t}_{\mathrm{T}}(\mathbf{x})\|, \quad \mathbf{t}_{\mathrm{T}}(\mathbf{x}) = \sum_{\alpha=1}^{2} [\mathbf{m}_{\alpha}(\mathbf{x}) \otimes \mathbf{m}_{\alpha}(\mathbf{x})] \cdot \mathbf{t}_{\mathscr{S}_-} \tag{20}$$

In 2D, the expression simplifies to the scalar form

$$t_{\mathrm{T}} = |\mathbf{m}(\mathbf{x}) \cdot \mathbf{t}_{\mathscr{S}_-}| \tag{21}$$

The criteria for stick and slip may be cast in the framework of classical plasticity theory using the yield function

$$f = t_{\mathrm{T}} + \mu t_{\mathrm{N}} \leqslant 0 \tag{22}$$

where μ is the coefficient of friction. Employing the associative flow rule defines the tangential relative sliding,

$$\dot{\mathbf{g}}_{\mathrm{T}} = \dot{\lambda} \frac{\partial f}{\partial \mathbf{t}_{\mathrm{T}}} = \dot{\lambda} \frac{\mathbf{t}_{\mathrm{T}}}{\|\mathbf{t}_{\mathrm{T}}\|} \tag{23}$$

Note that $\dot{\lambda}$ has the physical meaning of being the magnitude of the sliding velocity, i.e. $\dot{\lambda} = \|\dot{\mathbf{g}}_{\mathrm{T}}\|$. Finally, imposing the Kuhn–Tucker conditions once again defines the criteria for tangential stick/slip

$$\dot{\lambda} \geqslant 0, \quad f \leqslant 0, \quad \dot{\lambda} f = 0 \tag{24}$$

Stick condition pertains to the case $\dot{\lambda} = 0$ and $f < 0$, whereas slip condition pertains to the case $\dot{\lambda} > 0$ and $f = 0$.

The contact constitutive law enters into the variational equation through the surface integral $\mathscr{G}_{\mathrm{c}}$ see (14), which we rewrite below in terms of normal and tangential components of the weighting function $\boldsymbol{\eta}$,

$$\mathscr{G}_{\mathrm{c}} = \int_{\mathscr{S}} (\tilde{\eta}_{\mathrm{N}} t_{\mathrm{N}} + \tilde{\boldsymbol{\eta}}_{\mathrm{T}} t_{\mathrm{T}}) \, \mathrm{d}\Gamma \tag{25}$$

In this paper we impose a contact condition through the penalty method. For the normal component, we replace t_{N} by the constitutive expression

$$t_{\mathrm{N}} = \varepsilon_{\mathrm{N}} g_{\mathrm{N}} \tag{26}$$

where ε_{N} is a normal penalty parameter analogous to a normal spring that allows the contacting surfaces to slightly overlap (i.e. $g_{\mathrm{N}} < 0$). For the tangential component, the appropriate constitutive expression that allows for both stick and slip modes is

$$\dot{\mathbf{t}}_{\mathrm{T}} = \varepsilon_{\mathrm{T}} \left(\dot{\mathbf{g}}_{\mathrm{T}} - \dot{\lambda} \frac{\mathbf{t}_{\mathrm{T}}}{\|\mathbf{t}_{\mathrm{T}}\|} \right) \tag{27}$$

where ε_{T} is a tangential penalty parameter resembling a tangential spring constant. For very large ε_{T}, we recover the flow rule (23) under slip condition, which in turn readily degenerates to $\dot{\mathbf{g}}_{\mathrm{T}} = \mathbf{0}$ under stick condition when $\dot{\lambda} = 0$. For a finite ε_{T}, the above evolution equation mimics the

DOI: 10.1002/nme

predictor–corrector scheme of classical plasticity theory for which a return mapping algorithm can be readily implemented.

The return mapping algorithm follows that used in standard computational plasticity. We assume that $(\mathbf{t}_T)_n$, $\Delta\mathbf{g}_T$, and $g_N<0$ are given (allowing the surfaces to overlap slightly due to a finite value of ε_N), and we want to determine $(\mathbf{t}_T)_{n+1}\equiv\mathbf{t}_T$. As a starting point, we evaluate a traction predictor

$$\mathbf{t}_T^{tr}=(\mathbf{t}_T)_n+\varepsilon_T\Delta\mathbf{g}_T \tag{28}$$

and check whether $\|\mathbf{t}_T^{tr}\|+\mu\varepsilon_N g_N\leqslant 0$. If so, we accept the predictor as the final value (stick condition); otherwise, we use the backward implicit algorithm to correct for plastic sliding (slip condition),

$$\mathbf{t}_T=\mathbf{t}_T^{tr}-\varepsilon_T\Delta\lambda\frac{\mathbf{t}_T^{tr}}{\|\mathbf{t}_T^{tr}\|} \tag{29}$$

The incremental slip $\Delta\lambda$ is obtained by imposing the consistency condition $f=0$ and it takes the form

$$\Delta\lambda=\frac{\|\mathbf{t}_T^{tr}\|+\mu\varepsilon_N g_N}{\varepsilon_T} \tag{30}$$

Substituting back into (29) and simplifying give the final expression for tangential traction,

$$\mathbf{t}_T=-\mu\varepsilon_N g_N\frac{\mathbf{t}_T^{tr}}{\|\mathbf{t}_T^{tr}\|},\quad g_N<0 \tag{31}$$

As in the classical return mapping algorithm of computational plasticity, the direction of the final traction vector coincides with that of the elastic predictor.

4. MATRIX EQUATION AND LINEARIZATION

The continuous part of the displacement field is approximated by standard C^0 shape functions $N_I(\mathbf{x})$,

$$\overline{\mathbf{u}}(\mathbf{x})=\sum_{I\in N_{\text{nodes}}}N_I(\mathbf{x})\mathbf{d}_I=\mathbf{N}\mathbf{d} \tag{32}$$

where N_{nodes} is the set of total nodes and $\mathbf{d}_I$ is the regular displacement vector at node I. The discontinuous part of the displacement field is limited to the compact support of $M_{\mathscr{S}}(\mathbf{x})$, which we also assume to be discretized with FEs. Because all the FEs belonging in the support of $M_{\mathscr{S}}$ are intersected by the crack, they must be enhanced, and here we use the extended FE technique to enhance these elements.

The displacement field $\widetilde{\mathbf{u}}(\mathbf{x})$ is approximated by the same standard shape functions $N_I(\mathbf{x})$,

$$\widetilde{\mathbf{u}}(\mathbf{x})=\sum_{I\in N_{\text{enr}}}N_I(\mathbf{x})\mathbf{a}_I \tag{33}$$

where $\mathbf{a}_I$ is the vector of nodal enhancements and N_{enr} is the number of enriched nodes surrounding the crack. The displacement field $f^h(\mathbf{x})\widetilde{\mathbf{u}}(\mathbf{x})$ is interpolated according to the expression

$$f^h(\mathbf{x})\widetilde{\mathbf{u}}(\mathbf{x})=\sum_{I\in N_{\text{enr}}}N_I(\mathbf{x})H_{\mathscr{S}}(\mathbf{x}_I)\mathbf{a}_I \tag{34}$$

DOI: 10.1002/nme

Thus, the discontinuous part of the displacement field, $M_{\mathscr{S}}(\mathbf{x})\widetilde{\mathbf{u}}(\mathbf{x})$, takes the form

$$M_{\mathscr{S}}(\mathbf{x})\widetilde{\mathbf{u}}(\mathbf{x}) = \sum_{I \in N_{\text{enr}}} \widetilde{N}_{\text{I}}(\mathbf{x})\mathbf{a}_{\text{I}} = \widetilde{\mathbf{N}}\mathbf{a} \tag{35}$$

where

$$\widetilde{N}_{\text{I}}(\mathbf{x}) = N_{\text{I}}(\mathbf{x})[H_{\mathscr{S}}(\mathbf{x}) - H_{\mathscr{S}}(\mathbf{x}_{\text{I}})] \tag{36}$$

Although it is generally not possible to extract a closed-form expression for $f^h(\mathbf{x})$ from the interpolation given in (34), some essential features of the discontinuous displacement field are recovered from the above interpolations, as summarized below.

It can be seen from (35) that (a) the support of $M_{\mathscr{S}}(\mathbf{x})\widetilde{\mathbf{u}}(\mathbf{x})$ is the same as the support of $M_{\mathscr{S}}(\mathbf{x})$; (b) $M_{\mathscr{S}}(\mathbf{x})\widetilde{\mathbf{u}}(\mathbf{x})$ vanishes at all nodes $I \in N_{\text{enr}}$; and (c) the displacement jump on $\mathscr{S}$ is

$$[\![M_{\mathscr{S}}(\mathbf{x})\widetilde{\mathbf{u}}(\mathbf{x})]\!] = \widetilde{\mathbf{u}}(\mathbf{x}) = \sum_{I \in N_{\text{enr}}} N_{\text{I}}(\mathbf{x})\mathbf{a}_{\text{I}}, \quad \mathbf{x} \in \mathscr{S} \tag{37}$$

The above equation holds, provided the crack does not pass through any of the enriched nodes. Thus, although the additional degrees of freedom $\mathbf{a}$ are global, their effect on the element enrichment is purely local since they only serve to interpolate the displacement jump on $\mathscr{S}$. The fact that the discontinuous displacement field vanishes at the enriched nodes adds elegance to the formulation since the globally calculated displacements at the enriched nodes are the total final displacements. In other words, no 'blending' of the nodal displacements with the additional global degrees of freedom is required by the formulation [25, 39].

Crack tip elements require a special treatment since the crack is expected to terminate somewhere inside these elements. Following the approach in [24, 39], we show a typical crack tip constant strain triangular (CST) element in Figure 2. The crack passes through edge $\overline{13}$ and stops at point O inside this element. The direction of the crack is such that it will intersect edge $\overline{23}$; hence, we want no enrichments on edges $\overline{12}$ and $\overline{23}$. In other words, we enrich only side $\overline{13}$ along with the region $\Omega^{\text{e}*}_{\text{enr}} \subset \Omega^{\text{e}}_{\text{enr}}$ denoted by the shaded region in Figure 2. The displacement approximation in this case is given by

$$\mathbf{u}(\mathbf{x}) = \sum_{A=1}^{3} N_A(\mathbf{x})\mathbf{u}^{\text{e}}_A + N^*_1(\mathbf{x})[H_{\mathscr{S}}(\mathbf{x}) - H_{\mathscr{S}}(\mathbf{x}_1)]\mathbf{a}^{\text{e}}_1 \tag{38}$$

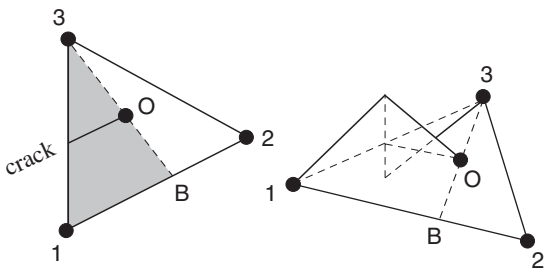

Figure 2. Enhancement of a crack tip CST element: shaded region is enriched (left) and representation of the jump function $M_{\mathscr{S}}$ on edge $\overline{13}$ (right).

DOI: 10.1002/nme

where $N_1(\mathbf{x})$ is the regular CST shape function for node 1 evaluated in Ω^{e*}_{enr}, with the properties that $N_1^*(\mathbf{x}_1)=1$ and $N_1^*(\mathbf{x}_3)=N_1^*(\mathbf{x}_B)=0$, see Figure 2 for point B.

The FE matrix equation consistent with variational equation (12) is

$$\mathbf{F}_{\mathrm{INT}}(\mathbf{d},\mathbf{a})=\mathbf{F}_{\mathrm{EXT}} \tag{39}$$

where

$$\begin{aligned}\mathbf{F}_{\mathrm{INT}}(\mathbf{d},\mathbf{a}) &= \int_\Omega \mathbf{B}^{\mathrm{T}}\boldsymbol{\sigma}(\mathbf{d},\mathbf{a})\,\mathrm{d}\Omega \\ \mathbf{F}_{\mathrm{EXT}} &= \int_\Omega \mathbf{N}^{\mathrm{T}}\mathbf{f}\,\mathrm{d}\Omega+\int_\Gamma \mathbf{N}^{\mathrm{T}}\mathbf{t}\,\mathrm{d}\Gamma\end{aligned} \tag{40}$$

The strain–displacement matrix operator $\mathbf{B}$ is defined from the regular shape function matrix $\mathbf{N}$ via the relation $\mathbf{B}=\boldsymbol{\nabla}^{\mathrm{s}}\mathbf{N}$. We made a slight abuse in the notation by denoting the Cauchy stresses in the vector form by the same symbol $\boldsymbol{\sigma}$. These stresses could depend on the vectors $\mathbf{d}$ and $\mathbf{a}$ in a non-linear way.

The FE matrix equation consistent with (13) is

$$\mathscr{F}_{\mathrm{INT}}(\mathbf{d},\mathbf{a})+\mathscr{G}_{\mathrm{INT}}(\mathbf{a})=\mathscr{F}_{\mathrm{EXT}} \tag{41}$$

where

$$\begin{aligned}\mathscr{F}_{\mathrm{INT}}(\mathbf{d},\mathbf{a}) &= \int_{\Omega^h\setminus\mathscr{S}} \widetilde{\mathbf{B}}^{\mathrm{T}}\boldsymbol{\sigma}(\mathbf{d},\mathbf{a})\,\mathrm{d}\Omega \\ \mathscr{G}_{\mathrm{INT}}(\mathbf{a}) &= \int_{\mathscr{S}} \mathbf{N}^{\mathrm{T}}\mathbf{t}_{\mathscr{S}_-}\,\mathrm{d}\mathscr{S} \\ \mathscr{F}_{\mathrm{EXT}} &= \int_{\Omega^h} \widetilde{\mathbf{N}}^{\mathrm{T}}\mathbf{f}\,\mathrm{d}\Omega+\int_{\Gamma^h} \widetilde{\mathbf{N}}^{\mathrm{T}}\mathbf{t}\,\mathrm{d}\Gamma\end{aligned} \tag{42}$$

The strain–displacement matrix operator $\widetilde{\mathbf{B}}$ is defined from the enhanced shape function matrix $\widetilde{\mathbf{N}}$ via the relation $\widetilde{\mathbf{B}}=\boldsymbol{\nabla}^{\mathrm{s}}\widetilde{\mathbf{N}}$. Note that $\mathscr{F}_{\mathrm{EXT}}$ and $\mathscr{F}_{\mathrm{INT}}$ use the enhanced shape function matrix, whereas $\mathscr{G}_{\mathrm{INT}}$ uses the regular one. In addition, because of the adopted frictional constitutive law, $\mathbf{t}_{\mathscr{S}_-}$ depends only on the displacement jump $\widetilde{\mathbf{u}}$ on $\mathscr{S}$. Therefore, $\mathscr{G}_{\mathrm{INT}}$ is a function only of the enrichment nodal vector $\mathbf{a}$ and not of the regular nodal displacement vector $\mathbf{d}$. Finally, note that all integrals in Equation (41) are evaluated over the elements crossed by the crack only.

To solve the non-linear problem, we write the coupled equations (39) and (41) in a standard residual form and iterate by Newton's method. The vector of unknowns and residual equation takes the form

$$\mathscr{D}=\begin{Bmatrix}\mathbf{d}\\ \mathbf{a}\end{Bmatrix},\quad \mathbf{r}(\mathscr{D})=\begin{Bmatrix}\mathbf{F}_{\mathrm{EXT}}-\mathbf{F}_{\mathrm{INT}}\\ \mathscr{F}_{\mathrm{EXT}}-\mathscr{F}_{\mathrm{INT}}-\mathscr{G}_{\mathrm{INT}}\end{Bmatrix} \tag{43}$$

Solving with Newton's method requires an evaluation of the algorithmic tangent operator

$$-\mathbf{r}'(\mathscr{D})=\begin{bmatrix}\mathbf{A}_{11} & \mathbf{A}_{12}\\ \mathbf{A}_{21} & \mathbf{A}_{22}\end{bmatrix} \tag{44}$$

DOI: 10.1002/nme

where

$$\mathbf{A}_{11}=\int_{\Omega}\mathbf{B}^{\mathrm{T}}\mathbf{D}\mathbf{B}\,\mathrm{d}\Omega,\quad \mathbf{A}_{12}=\int_{\Omega}\mathbf{B}^{\mathrm{T}}\mathbf{D}\widetilde{\mathbf{B}}\,\mathrm{d}\Omega$$
$$\mathbf{A}_{21}=\int_{\Omega^h}\widetilde{\mathbf{B}}^{\mathrm{T}}\mathbf{D}\mathbf{B}\,\mathrm{d}\Omega,\quad \mathbf{A}_{22}=\overline{\mathbf{A}}_{22}+\overline{\overline{\mathbf{A}}}_{22} \tag{45}$$
$$\overline{\mathbf{A}}_{22}=\int_{\Omega^h}\widetilde{\mathbf{B}}^{\mathrm{T}}\mathbf{D}\widetilde{\mathbf{B}}\,\mathrm{d}\Omega,\quad \overline{\overline{\mathbf{A}}}_{22}=\int_{\mathscr{S}}\mathbf{N}^{\mathrm{T}}\mathbf{E}\mathbf{N}\,\mathrm{d}\mathscr{S}$$

In general, the surface integral in $\mathbf{A}_{22}$ makes the matrix formulation unsymmetric since $\mathbf{E}$ is unsymmetric as demonstrated below.

In the geometrically linear regime, two sources of material non-linearities may arise. The first non-linearity may arise from the bulk response that renders the stress–strain matrix $\mathbf{D}$ non-constant throughout the iteration. Bulk plasticity is a typical source of this type of non-linearity, and $\mathbf{D}$ represents the algorithmic tangential matrix. The second non-linearity may emanate from tangential frictional sliding, represented in the above expression by the algorithmic tangent matrix $\mathbf{E}=\partial\mathbf{t}_{\mathscr{S}\_}/\partial\widetilde{\mathbf{u}}$ (appearing in $\mathbf{A}_{22}$ as a surface integral). The matrix $\mathbf{E}$ has a closed-form expression given below.

Let the traction vector on $\mathscr{S}$ be expressed in the following form:

$$\mathbf{t}_{\mathscr{S}\_}=t_{\mathrm{N}}\mathbf{n}+\mathbf{t}_{\mathrm{T}} \tag{46}$$

The gap function g_{N} and relative tangential movement g_{T} depend only on the displacement jump on $\mathscr{S}$ and are given by the expressions

$$g_{\mathrm{N}}=\mathbf{n}\cdot\widetilde{\mathbf{u}},\quad g_{\mathrm{T}}=\mathbf{m}\cdot\widetilde{\mathbf{u}}\quad\text{(for 2D)} \tag{47}$$

Hence, from (26) we obtain the derivative

$$\frac{\partial(t_{\mathrm{N}}\mathbf{n})}{\partial\widetilde{\mathbf{u}}}=\varepsilon_{\mathrm{N}}\mathbf{n}\otimes\mathbf{n} \tag{48}$$

The 2D tangential sliding restricts the kinematics to directions $\pm\mathbf{m}$, and if we rule out reverse sliding then $\mathbf{t}_{\mathrm{T}}^{\mathrm{tr}}/\|\mathbf{t}_{\mathrm{T}}^{\mathrm{tr}}\|=\mathbf{m}$. From (31) we obtain the derivative

$$\frac{\partial\mathbf{t}_{\mathrm{T}}}{\partial\widetilde{\mathbf{u}}}=-\mu\varepsilon_{\mathrm{N}}\mathbf{m}\otimes\mathbf{n} \tag{49}$$

Thus, a closed-form expression for matrix $\mathbf{E}$ is

$$\mathbf{E}=\varepsilon_{\mathrm{N}}(\mathbf{n}\mathbf{n}^{\mathrm{T}}-\mu\mathbf{m}\mathbf{n}^{\mathrm{T}}) \tag{50}$$

Note that matrix $\mathbf{E}$ is constant in this case due to a severe restriction in the kinematics of 2D frictional sliding. Sliding on a 3D surface entails less kinematical restrictions and produces a non-constant $\mathbf{E}$, which is also available in closed form.

Remark

Matrix $\mathbf{E}$ defined in (50) is unsymmetric due to the coupling of the normal and tangential tractions. In contrast, the equivalent matrix reported in [30] is symmetric since they ignored the coupling between the normal and tangential frictional forces.

DOI: 10.1002/nme

5. NUMERICAL EXAMPLES

We consider three numerical examples to investigate the performance of the proposed self-contact algorithm. The examples involve plane strain loading at infinitesimal deformation. In order to provide more meaningful discussions of the numerical results, we compare the solutions obtained from the penalty method with those obtained from the formulation of Dolbow *et al.* [26]. Dolbow *et al.* employed an iterative strategy called LATIN, LArge Time INcrement, a method proposed by Ladevèze [46] for solving non-linear evolution problems, see also [47]. Briefly, the LATIN procedure consists of partitioning equations into a (possibly) non-linear group **I** that is local in space and time, and a linear group **A** that is global in the spatial variables. A two-step approach, shown schematically in Figure 3, is employed by the LATIN method. The algorithm begins with an initial solution $\mathbf{s}_0^A$ in **A**. Non-linear update is determined by the solution $\mathbf{s}_0^I$ in **I**, which is then used to build the next approximate solution $\mathbf{s}_1^A$. The process is repeated sequentially until convergence is achieved.

Apart from the solutions provided by the penalty method and the Dolbow *et al.* approach, the comparison also focuses on the rates of convergence of the iterative schemes. Two convergence indicators were investigated: the L_2 norm of the residual force vector, $\|\mathbf{r}\|$, and the energy norm, $\mathbf{r}^{\mathrm{T}}\Delta\mathscr{D}$, where $\Delta\mathscr{D}$ is the search direction. For Newton's method, $\Delta\mathscr{D}_k$ is the search direction associated with residual vector $\mathbf{r}_k$. For the LATIN method, $\mathbf{r}_k$ is the residual force vector obtained by substituting the local solutions $\mathbf{s}_k^I$ into the kth global equations in the linear group **A**. For example, with reference to Figure 3, the initial residual force vector $\mathbf{r}_0$ would be the out-of-balance force created when the local traction vectors determined from the solution $\mathbf{s}_0^I$ are substituted into the global momentum balance equations originally used to solve for the global solution vector $\mathbf{s}_0^A$, and so on. Furthermore, for the LATIN method the search direction is calculated as $\Delta\mathscr{D}_k = \mathscr{D}_{k+1}^A - \mathscr{D}_k^A$, where the quantities on the right-hand side are determined from the global linear equation solve. Note that in Newton's method adopted in our proposed algorithm, the search directions $\Delta\mathscr{D}_k$, $\Delta\mathscr{D}_{k+1}$, etc. are calculated directly from the residual force vectors $\mathbf{r}_k$, $\mathbf{r}_{k+1}$, etc., whereas in the LATIN method adopted by Dolbow *et al.*, the iterations provide the cumulative solution vectors themselves, i.e. $\mathscr{D}_k$, $\mathscr{D}_{k+1}$, etc.

5.1. Square elastic domain with a crack

The FE mesh consists of 20 000 cross-diagonal CST elements defined by 10 201 nodes, as shown in Figure 4. The domain has in-plane dimensions of 1×1 m (square) and contains a 0.566 m center

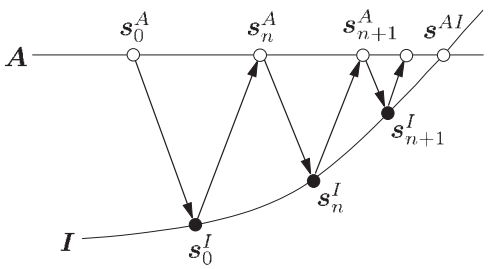

Figure 3. Schematic representation of LATIN iterative procedure (reproduced from [26]).

DOI: 10.1002/nme

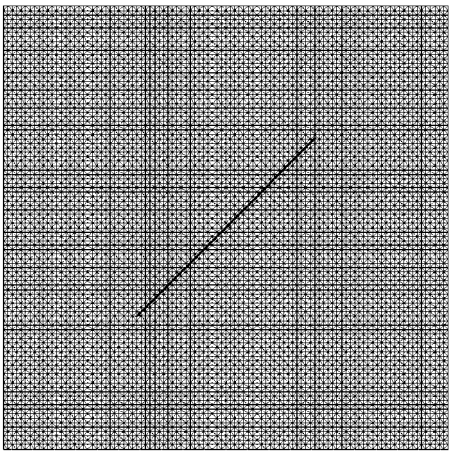

Figure 4. Finite element mesh with cross-diagonal CST elements. The mesh is 1×1 m (square) with a 0.566 m crack oriented at $\theta = \pi/4$ relative to the horizontal.

crack oriented at $\theta = \pi/4$ relative to the horizontal. In order for the crack to not intersect the nodes, the tips were specified at coordinates $(0.29999, 0.29998)$ and $(0.70002, 0.70001)$ m. The standard procedure of introducing more Gauss points in the vicinity of the crack was employed. The material is linearly elastic with Young's modulus $E = 10\,000$ MPa and the Poisson ratio $\nu = 0.30$. The crack is fully frictional with a coefficient of friction $\mu = 0.10$. We used the following regularization parameters for the crack: $\varepsilon_N = \varepsilon_T = 10^7$ MN/m^3 for the penalty method and $k = 10\,000$ MN/m^3 for the LATIN method (note that $\mathbf{k}_0 = k\mathbf{I}$). These regularization parameters generally influence the convergence rate of the iteration. For the penalty method, the higher the penalty parameter, the more accurate the contact condition, but a very high value of the penalty parameter could retard the convergence of the iteration; hence, some balance must be achieved. A similar statement may be made for the LATIN method, i.e. the regularization parameter k affects the rate of convergence of the iteration.

The body was deformed by applying a uniform vertical displacement at the top nodes while constraining the top and bottom surfaces from moving horizontally. For this example, we assumed that the crack could undergo frictional sliding but the crack tips could not advance. Figures 5 and 6 show the vertical and horizontal displacements predicted by the penalty and Dolbow *et al.* formulations after applying a uniform vertical displacement of -0.10 m at the top surface. For the penalty method with full Newton iteration, we used an error tolerance of $\|\mathbf{r}_k\|/\|\mathbf{r}_0\| < 10^{-10}$ based on the L_2 norm of the residual, and convergence to machine precision was achieved after only three iterations. This very stringent error tolerance could not be satisfied by the LATIN method; hence, we allowed up to 100 iterations. Because the LATIN iteration did not fully converge, the displacement profiles calculated by the two methods and shown in Figures 5 and 6 are only similar but not identical.

A more quantitative comparison of the penalty and Dolbow *et al.* solution is shown in Figure 7, which plots the total vertical reaction as a function of the imposed uniform vertical compression. The two solutions are nearly the same, but not identical. Given that the LATIN iterations have not completely dissipated the residual, the penalty solutions may be considered as 'more exact.' We

DOI: 10.1002/nme

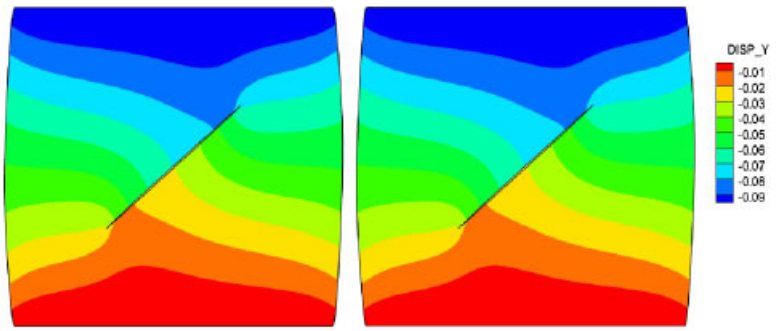

Figure 5. Contours of vertical displacement on deformed elastic solid with a crack: penalty method solution (left) and Dolbow *et al.* solution (right). Color bar in meters.

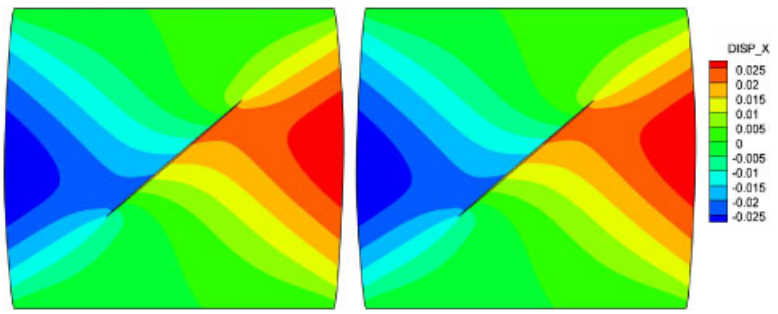

Figure 6. Contours of horizontal displacement on deformed elastic solid with a crack: penalty method solution (left) and Dolbow *et al.* solution (right). Color bar in meters.

should note that Figure 7 shows one-step solutions, not multi-step incremental solutions, to allow a direct comparison with the Dolbow *et al.* solutions. In other words, the solution at a vertical compression of 0.05 m corresponds to that generated in one time step from the starting value of zero, and not a continuation of the solution generated at a vertical compression of 0.03 m.

Tables I and II show convergence profiles based on the residual and energy norms of the Newton and LATIN iterations adopted by the penalty and Dolbow *et al.* formulations, respectively. As noted earlier, the LATIN method does not require a re-factor of the tangent operator, a computational advantage; however, the resulting rate of convergence exhibited by this method is much slower than that exhibited by the full Newton iteration. Table I suggests that after 100 iterations the LATIN method still has a convergence error of about 1% relative to the residual at iteration #1 (the residual dissipated between iteration #0 and #1 was dominated by the effects of the penalty parameters). In contrast, the Newton iteration has converged to machine precision after only three iterations. Note that the energy norm from the LATIN iteration switches in sign during the initial stage of iteration, and its absolute value decreases in a non-monotonic manner. Given that the solid was assumed to be a simple, linearly elastic material, it can be expected that the convergence rate of the LATIN iteration will only get worse in the presence of bulk plasticity.

DOI: 10.1002/nme

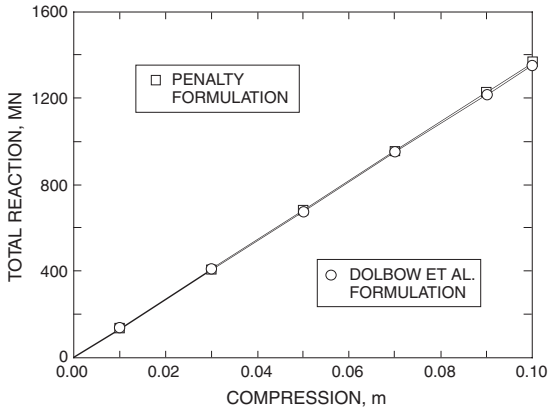

Figure 7. Comparison of solutions from penalty and Dolbow *et al.* formulations: total vertical reaction as a function of uniform vertical compression.

Table I. Convergence profiles of the Newton and LATIN iterations for elastic solid with a crack: residual norm $\|\mathbf{r}\|$.

Iteration	Newton	LATIN
0	1.791e+4	2.096e+2
1	7.838e+1	5.688e+1
2	6.529e−1	3.100e+1
3	2.168e−11	2.050e+1
4	—	1.589e+1
⋮		⋮
98		5.564e−1
99		5.558e−1
100		5.461e−1

Table II. Convergence profiles of the Newton and LATIN iterations for elastic solid with a crack: energy norm $\mathbf{r}^{\mathrm{T}}\Delta\mathscr{D}$.

Iteration	Newton	LATIN
0	1.779e+4	6.473e+1*
1	1.538e+1	1.011e+1
2	3.183e−8	2.503e−4*
3	—	5.964e−2*
4		6.140e−2*
⋮		⋮
98		1.195e−5
99		1.165e−5
100		1.137e−5

*Negative value.

DOI: 10.1002/nme

5.2. *Convergence studies*

We conducted a series of numerical simulations to assess the convergence of the formulation as a function of mesh refinement. We emphasize that the studies reported in this section focused only on the convergence of the Heaviside enrichment component of the formulation, and not on the crack tip kinematics. The latter is characterized by an infinite strain field, and therefore either an enhanced crack-tip interpolation [22] or a special FE [48] must be employed for such a case.

The problem is defined by a $1\,\mathrm{m}\times 1\,\mathrm{m}$ square elastic domain with a horizontal crack and deforming in plane strain. We considered four FE discretizations consisting of 200, 1250, 5000, and 20 000 CST elements (meshes 1–4, respectively), as shown in Figure 8. The bottom nodes were fixed, while the top nodes were given imposed non-uniform translations $\delta_y = 0.09x - 0.10\,\mathrm{m}$ (vertical) and $\delta_x = 0.05\,\mathrm{m}$ (horizontal), where $0 \leqslant x \leqslant 1.0\,\mathrm{m}$. All of the material parameters were the same as in Example 1 except that the penalty parameter was selected to vary linearly with element size, $\varepsilon_\mathrm{N} = \varepsilon_\mathrm{T} = Ch$, where $C = 10^9$ is a constant of proportionality and $h = 0.10$, 0.04, 0.02, and 0.01 m, for meshes 1–4, respectively. Note that since the penalty parameter has the physical equivalence of a spring constant, it had to be adjusted to reflect the length scale of the FE discretization.

The convergence studies focused on the normal contact stress and slip distributions on the crack (the contact shear stress is simply the normal contact stress multiplied by the coefficient of

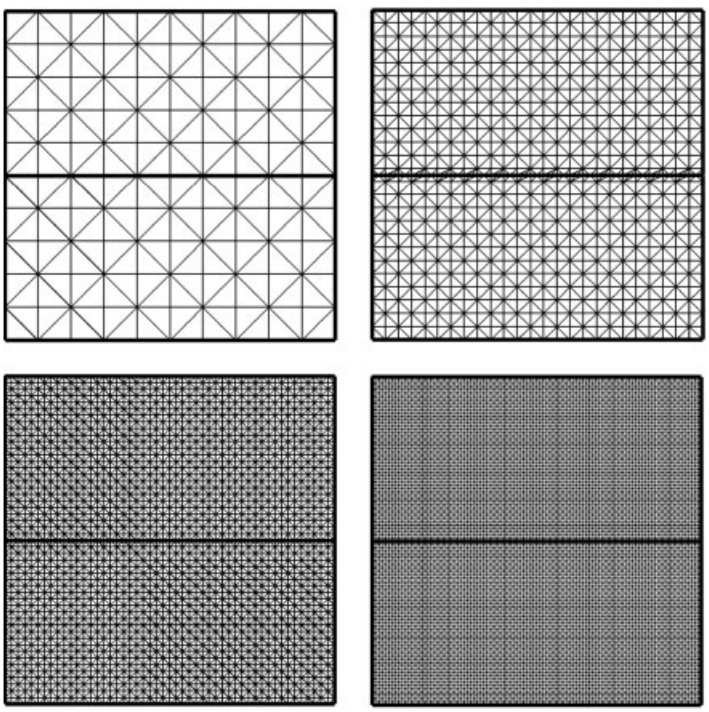

Figure 8. Convergence studies for a square elastic domain with a horizontal crack: meshes 1 (upper left), 2 (upper right), 3 (lower left), and 4 (lower right), defined by 200, 1250, 5000, and 20 000 CST elements, respectively.

DOI: 10.1002/nme

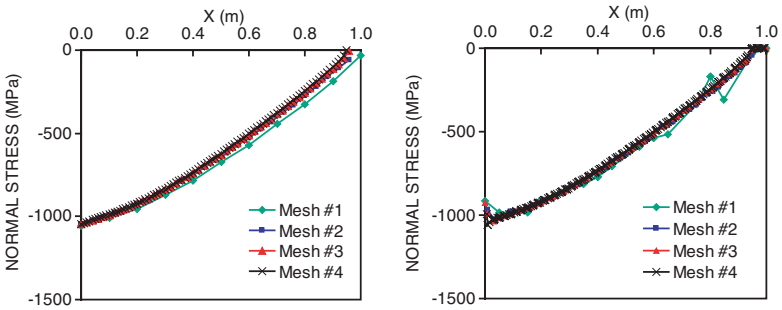

Figure 9. Convergence of normal stresses for a square elastic domain with a horizontal crack: penalty/Newton method (left) and LATIN method (right).

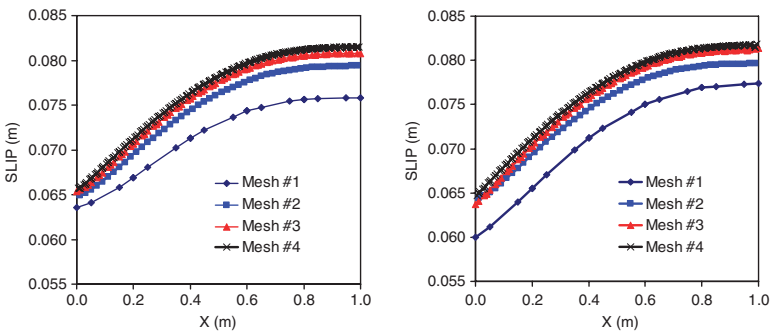

Figure 10. Convergence of slip for a square elastic domain with a horizontal crack: penalty method/Newton method (left) and LATIN method (right).

friction). To evaluate the contact stress from a given contact force, we performed simple projections of the contact forces onto the enriched degrees of freedom, collected the forces on the enriched nodes, and then projected them back to the contact surfaces. Note that this simple operation is a post-processing scheme and does not affect the global system of equations. The above procedure is essentially equivalent to the domain integral technique described in [49].

Figure 9 shows the distribution of normal contact stresses along the crack calculated by the penalty/Newton and LATIN iterative solutions. The maximum contact stresses occurred at $x=0$ where the imposed vertical compression was maximum. The normal contact stresses are nearly insensitive to mesh refinement. The LATIN iteration did not converge sufficiently after 100 iterations for the coarse mesh, and this might have been responsible for the slight oscillations observed in the normal stresses.

Figure 10 shows the slip distributions predicted by the two methods for the same convergence studies. The rates of convergence appear to be the same, although the LATIN solution for the coarse mesh exhibited larger errors. Table III summarizes the calculated vertical component of resultant force (i.e. reaction) on top of the mesh. We recall that we conducted one-step simulations, which did not permit a detailed load–displacement curve. Nevertheless, the results presented in Table III suggest a monotonic mesh convergence.

DOI: 10.1002/nme

Table III. Mesh convergence studies: total vertical reaction (MN) at the top of the square elastic domain.

	Penalty	LATIN
Mesh 1	636.6678	617.6726
Mesh 2	601.6237	596.0894
Mesh 3	590.0530	588.3292
Mesh 4	584.0989	583.3224

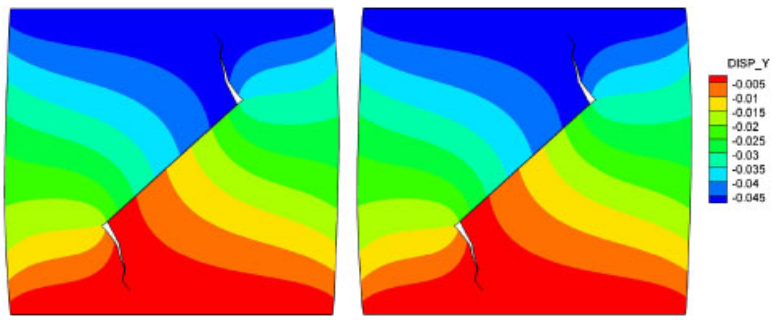

Figure 11. Contours of vertical displacement on deformed elastic solid with advancing crack tips: penalty method solution (left) and Dolbow *et al.* solution (right). Color bar in meters.

5.3. Square elastic domain with advancing crack tips

The example involves a re-analysis of Example 1, assuming this time that the tips of the crack were free to advance. We employed linear elastic fracture mechanics (LEFM) and compared the equivalent stress intensity factor $K_{\mathrm{I}}^{\mathrm{eq}}$ with the critical stress intensity factor K_{c} (also called the fracture toughness), as well as activated crack growth when $K_{\mathrm{I}}^{\mathrm{eq}} \geqslant K_{\mathrm{c}}$. For convenience, we assumed an unstable crack growth and propagated the crack according to a predefined length of 0.04 m at each step. We propagated the crack in the direction of the maximum hoop, or circumferential, stress, which is determined by using the stress intensity factors K_{I} and K_{II} in LEFM. The propagation direction in terms of the stress intensity factors is given by

$$\theta_{\mathrm{c}} = 2 \arctan \frac{1}{4} \left(\frac{K_{\mathrm{I}}}{K_{\mathrm{II}}} \pm \sqrt{\frac{K_{\mathrm{I}}}{K_{\mathrm{II}}} + 8} \right) \tag{51}$$

For purposes of calculating the mixed-mode stress intensity factors, we assumed a radius of $r_d = 0.025$ m for the interaction integral. In addition, we set $K_{\mathrm{c}} = 30$ so that the crack stops growing at the end of step #6. We allowed up to 200 LATIN iterations per step to achieve proper convergence.

Figures 11 and 12 show contours of displacements predicted by the penalty and Dolbow *et al.* solutions after applying a uniform vertical displacement of -0.05 m on top of the mesh (horizontal displacements at the top and bottom nodes were zero). The displacements are indistinguishable for plotting purposes, which can be attributed to the fact that we allowed the LATIN iterations to converge properly. However, that LATIN did not converge to machine precision still created some

DOI: 10.1002/nme

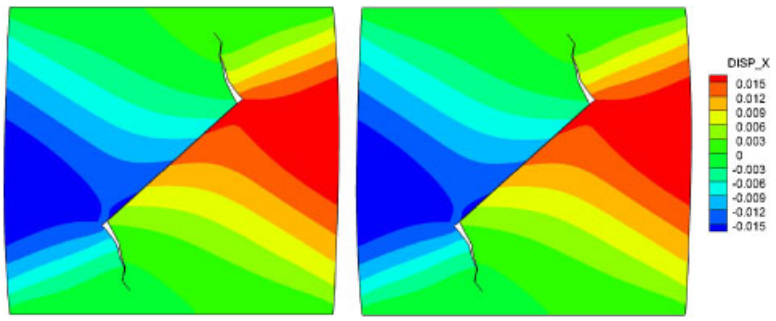

Figure 12. Contours of horizontal displacement on deformed elastic solid with advancing crack tips: penalty method solution (left) and Dolbow *et al.* solution (right). Color bar in meters.

Table IV. Stress intensity factors for modes I and II fracture calculated by the penalty method.

	Mode I	Mode II
Step 1		
LCT	−42.82	−265.36
RCT	−48.99	−249.79
Step 2		
LCT	170.72	−3.94
RCT	171.40	−0.65
Step 3		
LCT	119.58	23.59
RCT	122.56	21.97
Step 4		
LCT	84.67	−6.01
RCT	85.46	−6.04
Step 5		
LCT	51.01	15.29
RCT	50.54	15.71
Step 6		
LCT	20.08	−14.59
RCT	21.02	−15.05

LCT, left crack tip; RCT, right crack tip.

numerical discrepancies as can be observed from the calculated stress intensity factors shown in Tables IV and V.

Tables VI and VII show the convergence profiles of the Newton and LATIN iterations. For the penalty method, the number of iterations increased slightly as the crack propagated because the more complicated geometry of the crack made the initial guess quite far from the solution. Nevertheless, Newton's method still converged to machine precision in less than 10 iterations.

5.4. Square elastoplastic domain with a crack

The final example demonstrates the performance of the penalty method for frictional crack propagation in the presence of bulk plasticity. The problem investigated is the same as in Example 1

DOI: 10.1002/nme

Table V. Stress intensity factors for modes I and II fracture calculated by the Dolbow *et al.* method.

	Mode I	Mode II
Step 1		
LCT	−51.44	−251.49
RCT	−55.04	−251.74
Step 2		
LCT	171.54	1.93
RCT	171.21	1.93
Step 3		
LCT	119.72	20.20
RCT	122.46	19.72
Step 4		
LCT	84.60	−5.51
RCT	85.54	−4.61
Step 5		
LCT	50.92	15.28
RCT	51.17	13.90
Step 6		
LCT	20.02	−14.62
RCT	21.51	−13.17

LCT, left crack tip; RCT, right crack tip.

Table VI. Convergence profiles of the Newton and LATIN iterations for elastic solid with advancing crack tips: residual norm $\|\mathbf{r}\|$.

Iteration	Newton	LATIN
0	8.956e+3	1.848e+2
1	4.929e+1	6.054e+1
2	5.784e+1	4.013e+1
3	5.346e+1	2.845e+1
⋮		⋮
8	2.759e−1	1.357e+1
9	1.124e−12	1.214e+1
10	—	1.102e+1
⋮		⋮
198		8.000e−1
199		7.959e−1
200		7.900e−1

except that we assumed the solid to be an elastic–perfectly plastic material yielding according to a non-associated Drucker–Prager yield criterion. The yield criterion is

$$\sqrt{\tfrac{2}{3}}q-(\alpha-\beta p)=0 \tag{52}$$

where $q=\sqrt{3/2}\|\mathbf{s}\|$ is the Mises stress, $\mathbf{s}$ is the deviatoric component of $\boldsymbol{\sigma}$, and $p=\mathrm{tr}(\boldsymbol{\sigma})/3$ is the mean normal stress (negative for compression). The material parameters are $\alpha=17$ and $\beta=1.0$.

DOI: 10.1002/nme

Table VII. Convergence profiles of the Newton and LATIN iterations for elastic solid with advancing crack tips: energy norm $\mathbf{r}^{\mathrm{T}}\Delta\mathscr{D}$.

Iteration	Newton	LATIN
0	4.449e+3	3.089e+1
1	4.113e+0	2.646e−1
2	6.458e−1	1.738e−1*
3	7.473e−1	1.409e−2*
⋮		⋮
7	2.344e−4	2.918e−2
8	7.979e−6	2.365e−2
9	—	1.924e−2
⋮		⋮
198		2.454e−5
199		2.420e−5
200		2.387e−5

*Negative value.

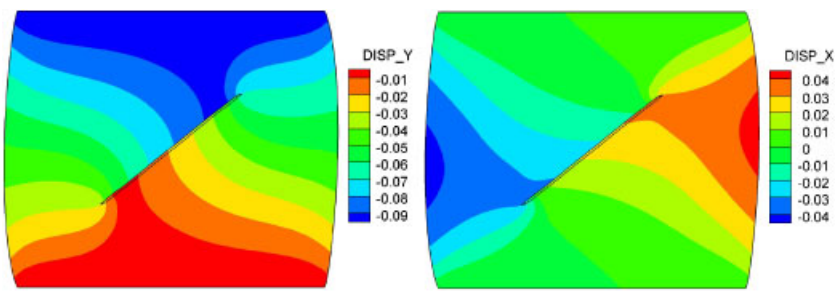

Figure 13. Displacement contours on deformed elastoplastic solid with a crack solved by the standard penalty formulation. Contours generated by the augmented Lagrangian technique are nearly identical. Color bar in meters.

The plastic potential has a similar form to the yield function except that we replaced the continuum frictional parameter β with the continuum dilatancy parameter $b=0.8$.

We did not implement the Dolbow *et al.* formulation for the elastoplastic problem. However, we have also implemented the augmented Lagrangian technique [45] to assess the impact of the penalty parameters on the accuracy of our solution. Figures 13 and 14 show, respectively, the contours of displacement and deviatoric plastic strain after applying a vertical compression of 0.10 m. Results generated by the standard penalty formulation and the augmented Lagrangian technique (with three augmentations per load step) are indistinguishable but not identical. For brevity, we show only the displacement contours generated by the standard penalty formulation in Figure 13. Figure 14 presents two seemingly identical results generated by the two approaches, indicating the efficacy and adequacy of the standard penalty formulation for this particular example. Figure 14 also shows that bulk plasticity is localized around the crack tips. A possible criterion to propagate the crack

DOI: 10.1002/nme

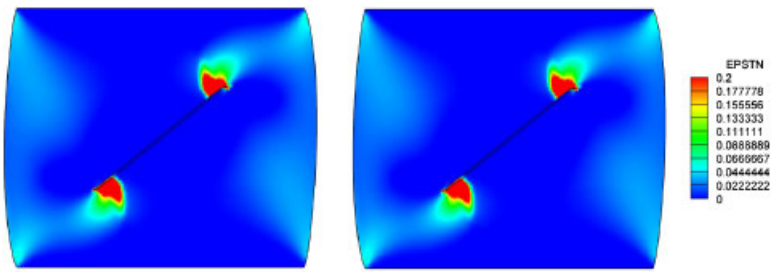

Figure 14. Cumulative deviatoric plastic strain on deformed elastoplastic solid with a crack at a vertical compression of 0.10 m: standard penalty formulation (left) and augmented Lagrangian formulation with three augmentations per time step (right). Note: Blue is the elastic region.

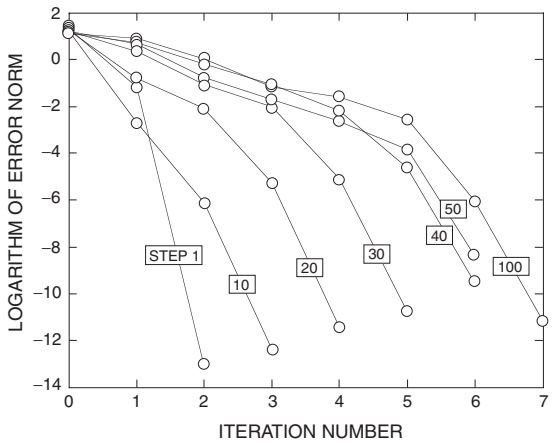

Figure 15. Convergence profiles based on the residual norm of Newton's iterations for non-associated Drucker–Prager elastoplastic solid with a frictional crack solved by the standard penalty formulation. Numbers inside boxes are step numbers. The number of iterations increased with increasing plastic deformation, but in all cases Newton's method converged to machine precision in seven iterations or less.

in the yielded zone would be to use classical bifurcation theory [50, 51]; we defer this aspect for further research. Finally, Figures 15 and 16 demonstrate the performance of Newton's method for the standard penalty and augmented Lagrangian approaches, respectively. Despite the presence of bulk plasticity, all steps converged to machine precision in seven iterations or less.

6. CONCLUSION

We have presented an incremental quasi-static contact algorithm for path-dependent frictional crack propagation in the framework of the extended FE method. The variational formulation differs from the existing framework for frictional crack propagation in that the enhancements are expressed in terms of the relative slip, and not in terms of the total displacements on each side of the crack. Furthermore, the weak form automatically satisfies traction continuity. The proposed variational

DOI: 10.1002/nme

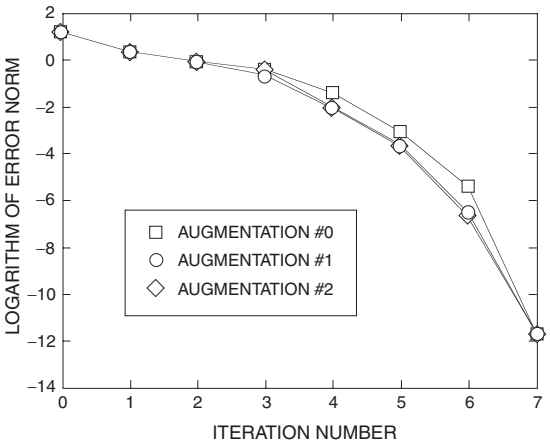

Figure 16. Convergence profiles based on the residual norm of Newton's iterations for non-associated Drucker–Prager elastoplastic solid with a frictional crack solved by the augmented Lagrangian approach. Profiles pertain to three augmentations at step 100 of the elastoplastic solution.

formulation mimics that commonly utilized for strong discontinuity kinematics, suggesting that local and global enrichments are members of similar families of embedded discontinuity methods.

The variational formulation embeds the algorithm of non-linear contact mechanics directly into the enhancement equations. The algorithm defines master and slave sides that satisfy unilateral constraints imposed by frictional contact. The contributions of frictional contact are expressed in terms of internal nodal forces, which, along with the bulk non-linear responses, are linearized consistently for iteration with full Newton's method. The iterative approach delivers optimal quadratic convergence rate and allows the solution to achieve accuracy to machine precision.

Crack propagation is an instability problem requiring high-fidelity calculations. For incremental path-dependent loading, residuals from insufficient convergence of the iterations are known to propagate and 'contaminate' the subsequent solutions. Stability problems such as frictional crack propagation are very sensitive to these errors. The method proposed in this study provides a means for conducting high-fidelity simulations at reasonable computing costs.

ACKNOWLEDGEMENTS

This study is supported by the U.S. Department of Energy Grant No. DE-FG02-03ER15454 and National Science Foundation Grant No. CMG-0417521 (Collaborations in Mathematical Geosciences). We thank graduate student Pablo F. Sanz for assisting in the implementation of the contact algorithm. We also thank the two anonymous reviewers for their reviews. The first author acknowledges a Stanford Graduate Fellowship support.

REFERENCES

1. Andrade JE, Borja RI. Capturing strain localization in dense sands with random density. *International Journal for Numerical Methods in Engineering* 2006; **67**:1531–1564.
2. Aydin A, Borja RI, Eichhubl P. Geological and mathematical framework for failure modes in granular rock. *Journal of Structural Geology* 2006; **28**:83–98.

DOI: 10.1002/nme

3. Baxevanis T, Papamichos E, Flornes O, Larsen I. Compaction bands and induced permeability reduction in Tuffeau de Maastricht calcarenite. *Acta Geotechnica* 2006; **1**:123–135.
4. Bažant ZP, Planas J. *Fracture and Size Effect in Concrete and Other Brittle Materials*. CRC Press: New York, 1998.
5. Borja RI. Conditions for instabilities in collapsible solids including volume implosion and compaction banding. *Acta Geotechnica* 2006; **1**:107–122.
6. Borja RI. Conditions for liquefaction instability in fluid saturated granular soils. *Acta Geotechnica* 2006; **1**: 211–224.
7. Borja RI, Andrade JE. Critical state plasticity. Part VI: meso-scale finite element simulation of strain localization in discrete granular materials. *Computer Methods in Applied Mechanics and Engineering* 2006; **195**:5115–5140.
8. Borja RI, Aydin A. Computational modeling of deformation bands in granular media. I. Geological and mathematical framework. *Computer Methods in Applied Mechanics and Engineering* 2004; **193**:2667–2698.
9. Borja RI. Computational modeling of deformation bands in granular media. II. Numerical simulations. *Computer Methods in Applied Mechanics and Engineering* 2004; **193**:2699–2718.
10. Holcomb D, Rudnicki JW, Issen KA, Sternlof K. Compaction localization in the Earth and the laboratory: state of the research and research directions. *Acta Geotechnica* 2007; **2**:1–15.
11. Issen KA, Rudnicki JW. Conditions for compaction bands in porous rock. *Journal of Geophysical Research* 2000; **105**:21529–21536.
12. Nádai A. *Plasticity*. McGraw-Hill: New York, 1931.
13. Paterson MS, Wong T-F. *Experimental Rock Deformation—The Brittle Field* (2nd edn). Springer: New York, 2005.
14. Armero F, Garikipati K. Recent advances in the analysis and numerical simulation of strain localization in inelastic solids. In *Proceedings of Computational Plasticity IV*, Owen DRJ, Oñate E, Hinton E (eds). CIMNE: Barcelona, Spain, 1995; 547–561.
15. Borja RI. A finite element model for strain localization analysis of strongly discontinuous fields based on standard Galerkin approximation. *Computer Methods in Applied Mechanics and Engineering* 2000; **190**:1529–1549.
16. Borja RI, Regueiro RA. Strain localization in frictional materials exhibiting displacement jumps. *Computer Methods in Applied Mechanics and Engineering* 2001; **190**:2555–2580.
17. Borja RI. Finite element simulation of strain localization with large deformation: capturing strong discontinuity using a Petrov–Galerkin multiscale formulation. *Computer Methods in Applied Mechanics and Engineering* 2002; **191**:2949–2978.
18. Larsson R, Runesson K, Sture S. Embedded localization band in undrained soil based on regularized strong discontinuity theory and FE analysis. *International Journal of Solids and Structures* 1996; **33**:3081–3101.
19. Regueiro RA, Borja RI. Plane strain finite element analysis of pressure-sensitive plasticity with strong discontinuity. *International Journal of Solids and Structures* 2001; **38**:3647–3672.
20. Simo JC, Oliver J, Armero F. An analysis of strong discontinuities induced by strain-softening in rate-independent inelastic solids. *Computational Mechanics* 1993; **12**:277–296.
21. Simo JC, Oliver J. A new approach to the analysis and simulation of strain softening in solids. In *Fracture and Damage in Quasibrittle Structures*, Bažant ZP, Bittnar Z, Jirásek M, Mazars J (eds). E&FN Spon: London, 1994.
22. Belytschko T, Black T. Elastic crack growth in finite elements with minimal remeshing. *International Journal for Numerical Methods in Engineering* 1999; **45**:601–620.
23. Belytschko T, Moës N, Usui S, Parimi C. Arbitrary discontinuities in finite elements. *International Journal for Numerical Methods in Engineering* 2001; **50**:993–1013.
24. Belytschko T, Hao C, Xu J, Zi G. Dynamic crack propagation based on loss of hyperbolicity and a new discontinuous enrichment. *International Journal for Numerical Methods in Engineering* 2003; **58**:1873–1905.
25. Chessa Z, Wang H, Belytschko T. On the construction of blending elements for local partition of unity enriched finite elements. *International Journal for Numerical Methods in Engineering* 2003; **57**:1015–1038.
26. Dolbow J, Möes N, Belytschko T. An extended finite element method for modeling crack growth with frictional contact. *Computer Methods in Applied Mechanics and Engineering* 2001; **190**:6825–6846.
27. Elguedj T, Gravouil A, Combescure A. A mixed augmented Lagrangian-extended finite element method for modelling elastic–plastic fatigue crack growth with unilateral contact. *International Journal for Numerical Methods in Engineering* 2007; **71**:1569–1597.
28. Ji H, Dolbow JE. On strategies for enforcing interfacial constraints and evaluating jump conditions with the extended finite element method. *International Journal for Numerical Methods in Engineering* 2004; **61**:2508–2535.
29. Khoei AR, Shamloo A, Azami AR. Extended finite element method in plasticity forming of powder compaction with contact friction. *International Journal of Solids and Structures* 2006; **43**:5421–5448.

DOI: 10.1002/nme

30. Khoei AR, Nikbakht M. An enriched finite element algorithm for numerical computation of contact friction problems. *International Journal of Mechanical Sciences* 2007; **49**:183–199.
31. Kim TY, Dolbow J, Laursen T. A mortared finite element method for frictional contact on arbitrary interfaces. *Computational Mechanics* 2007; **39**:223–235.
32. Moës N, Dolbow J, Belytschko T. A finite element method for crack growth without remeshing. *International Journal for Numerical Methods in Engineering* 1999; **46**:131–150.
33. Moës N, Belytschko T. Extended finite element method for cohesive crack growth. *Engineering Fracture Mechanics* 2002; **69**:813–833.
34. Samaniego E, Belytschko T. Continuum–discontinuum modelling of shear bands. *International Journal for Numerical Methods in Engineering* 2005; **62**:1857–1872.
35. Sukumar N, Prevost JH. Modeling quasi-static crack growth with the extended finite element method. Part I: computer implementation. *International Journal of Solids and Structures* 2003; **40**:7513–7537.
36. Sukumar N, Moës N, Moran B, Belytschko T. Extended finite element method for three-dimensional crack modelling. *International Journal for Numerical Methods in Engineering* 2000; **48**:1549–1570.
37. Sukumar N, Chopp DL, Moës N, Belytschko T. Modeling holes and inclusions by level sets in the extended finite-element method. *Computer Methods in Applied Mechanics and Engineering* 2001; **190**:6183–6200.
38. Wells GN, de Borst R, Sluys LJ. A consistent geometrically non-linear approach for delamination. *International Journal for Numerical Methods in Engineering* 2002; **54**:1333–1355.
39. Zi G, Belytschko T. New crack-tip elements for XFEM and applications to cohesive cracks. *International Journal for Numerical Methods in Engineering* 2003; **57**:2221–2240.
40. Laursen TA, Simo JC. A continuum-based finite element formulation for the implicit solution of multibody, large deformation frictional contact problems. *International Journal for Numerical Methods in Engineering* 1993; **36**:3451–3485.
41. Sanz PF, Borja RI, Pollard DD. Mechanical aspects of thrust faulting driven by far-field compression and their implications for fault geometry. *Acta Geotechnica* 2007; **2**:17–31.
42. Wriggers P. *Computational Contact Mechanics*. Wiley: Chichester, 2002.
43. Geniaut S. *Approche X-FEM pour la fissuration sous contact des structures industrielles*. Thèse de Doctorat de l'Ecole Centrale de Nantes, France, 2006.
44. Geniaut S, Massin P, Moës N. A stable 3D contact formulation using X-FEM. *European Journal for Computational Mechanics* 2007; **16**:259–275.
45. Simo JC, Laursen TA. An augmented Lagrangian treatment of contact problems involving friction. *Computers and Structures* 1992; **42**:97–116.
46. Ladevèze P. *Non-linear Computational Structural Mechanics*. Springer: New York, 1999.
47. Ribeaucourt R, Baietto-Dubourg MC, Gravouil A. A new fatigue frictional contact crack propagation model with the coupled X-FEM/LATIN method. *Computer Methods in Applied Mechanics and Engineering* 2007; **196**:3230–3247.
48. Rice JR, Tracey DM. Computational fracture mechanics. In *Numerical and Computer Methods in Structural Mechanics*, Fenves SJ *et al.* (eds). Academic Press: New York, 1973; 585–623.
49. Mourad HM, Dolbow J, Harari I. Bubble-stabilized finite element method for Dirichlet constraints on embedded interfaces. *International Journal for Numerical Methods in Engineering* 2006; **69**:772–793.
50. Borja RI. Bifurcation of elastoplastic solids to shear band mode at finite strain. *Computer Methods in Applied Mechanics and Engineering* 2002; **191**:5287–5314.
51. Rudnicki JW, Rice JR. Conditions for the localization of deformation in pressure-sensitive dilatant materials. *Journal of the Mechanics and Physics of Solids* 1975; **23**:371–394.

DOI: 10.1002/nme